

Sparse covariate-driven factorization of high-dimensional brain connectivity with application to site effect correction

Rongqian Zhang^{1*}, Elena Tuzhilina¹, Jun Young Park^{1,2†}

¹*Department of Statistical Sciences, University of Toronto, Toronto, ON, Canada*

²*Department of Psychology, University of Toronto, Toronto, ON, Canada*

Abstract. Large-scale neuroimaging studies often collect data from multiple scanners across different sites, where variations in scanners, scanning procedures, and other conditions across sites can introduce artificial site effects. These effects may bias brain connectivity measures, such as functional connectivity (FC), which quantify functional network organization derived from functional magnetic resonance imaging (fMRI). How to leverage high-dimensional network structures to effectively mitigate site effects has yet to be addressed. In this paper, we propose SLACC (Sparse LAtent Covariate-driven Connectome) factorization, a multivariate method that explicitly parameterizes covariate effects in latent subject scores corresponding to sparse rank-1 latent patterns derived from brain connectivity. The proposed method identifies localized site-driven variability within and across brain networks, enabling targeted correction. We develop a penalized Expectation-Maximization (EM) algorithm for parameter estimation, incorporating the Bayesian Information Criterion (BIC) to guide optimization. Extensive simulations validate SLACC's robustness in recovering the true parameters and underlying connectivity patterns. Applied to the Autism Brain Imaging Data Exchange (ABIDE) dataset, SLACC demonstrates its ability to reduce site effects. The R package to implement our method is publicly available.

Keywords: Batch effects; blind-source separation; functional connectivity; sparsity; low-rank; tensor.

*Current affiliation: Department of Epidemiology and Biostatistics, The University of California San Francisco, San Francisco, CA, United States.

†Corresponding author: juny.park@utoronto.ca

1 Introduction

Brain magnetic resonance imaging (MRI) offers a powerful tool for studying brain activity and structure in both healthy and clinical populations. One of its key applications is functional connectivity (FC) derived from functional MRI (fMRI), which quantifies the statistical dependencies between blood-oxygen-level-dependent (BOLD) signals measured over time from two spatially distinct brain regions (Biswal et al., 1995; Friston et al., 1993; Greicius et al., 2003). FC has been extensively used to investigate brain network organization and its alterations due to neurodevelopment, neuropsychiatric/ neurological disease progression or treatment (Zonneveld et al., 2019; Van Den Heuvel & Pol, 2010; Fox & Greicius, 2010). Common measures of FC include the Pearson correlation (Fox et al., 2005), partial correlation (Marrelec et al., 2006) and mutual information (Z. Wang et al., 2015).

Despite the widespread use of FC in neuroimaging studies, multi-site data collection introduces significant challenges to its data quality. In large-scale fMRI studies, data collection often involves multiple sites and scanners, which can lead to artificial site effects due to differences in scanner models, scanning protocols, and other local conditions. These effects can increase unwanted variations in FC, which can confound analyses and limit the generalizability and reproducibility of findings. Several statistical harmonization methods have been developed to identify, characterize, and mitigate site effects in neuroimaging data, enabling the construction of harmonized datasets across multiple sites. ComBat, a prominent approach originally proposed for genomics by Johnson et al. (2007), characterizes site effects as an additive (mean) and a multiplicative (variance) site effect for each feature. It has shown great potential for neuroimaging modalities, including diffusion tensor imaging (DTI) (Fortin et al., 2017), cortical thickness (Fortin et al., 2018), and functional connectivity (Yu et al., 2018). More recent harmonization methods, such as CovBat and RELIEF, expand the scope of statistical harmonization to address not only mean-variance differences but also heterogeneity in covariances across sites (A. A. Chen, Beer, et al., 2022; Zhang et al., 2023, 2024).

Despite the advancements in harmonization techniques, existing harmonization methods for brain connectivity data remain limited, ignoring the structure of FC that is represented as a symmetric matrix, where each element corresponds to the connection strength, or edge, between two brain regions. Many methods are based on applying existing harmonization approaches to the vectorized connectivity matrices (Yu et al., 2018; A. A. Chen, Srinivasan, et al., 2022), thus suffer from ignoring important network properties inherent to fMRI. This creates difficulties in interpreting how site effects have been identified and corrected within and across brain networks, potentially leading to suboptimal harmonization.

In brain network analysis, blind source separation (BSS) and independent component analysis (ICA) have been used in recent methodological advances to decompose FC into low-rank and sparse structures. These structures identify patterns between and within functional networks, while simultaneously quantifying the strength of these patterns in each subject (Eavani et al., 2015; Cai et al., 2017; Y. Wang & Guo, 2023). Other studies aim to explore the relationships between

connectivity patterns and clinical or demographic factors, as well as other imaging modalities, typically within a linear modeling framework (Sun & Li, 2017; Zhao et al., 2021; Zhao & Zhao, 2025; Park, 2025). The connectivity matrix is either used as a high-dimensional predictor to examine its associations with clinical or demographic variables or other imaging modalities as the response, or the connectivity matrix itself is modeled as the response to these variables. To reduce the number of parameters, these models often impose low-rank structures either on the FC matrix itself (Zhao et al., 2021; Zhao & Zhao, 2025) or on the regression parameters (Sun & Li, 2017). In a more generalized dimension reduction framework, Lock & Li (2018) propose a likelihood-based latent variable representation for CANDECOMP/PARAFAC (CP) decomposition on tensors of arbitrary dimensions, where the latent variables are informed by covariates. However, as Zhao et al. (2021) and Park (2025) noted, incorporating the high dimensionality of the whole-brain network remains an important methodological and practical challenge.

In this paper, we hypothesize that leveraging recent advances in latent variable modeling, particularly in low-rank matrix/tensor factorization techniques, would be beneficial for improving the harmonization of brain connectivity data. Building on this, we propose a covariate-driven latent factor model for brain connectivity, which decomposes connectivity data into a linear combination of low-rank, sparse connectivity patterns, weighted by covariate factors. The sparsity assumption is motivated by two key considerations. First, the human brain is organized into distinct functional networks, each involving a relatively small number of regions (Salvador et al., 2005). Sparse connectivity patterns provide a parsimonious representation of these localized connections between brain regions (Eavani et al., 2015). Second, because connectivity matrices are high-dimensional, enforcing sparsity in latent patterns reduces the effective number of parameters, resulting in more stable and reliable estimates while preventing the risk of spurious findings (Y. Wang & Guo, 2023).

By embedding site and covariate effects into these latent factors, our model aims to identify and correct for localized site-specific heterogeneity within and across brain networks, while also accounting for biological effects from covariates. Our model achieves a more efficient and flexible representation of multi-site connectivity matrices by explicitly using site effects to drive the decomposition, avoiding the need for vectorization and thus preserving the network properties and the dependence structure of the connectivity matrix. Moreover, incorporating low-rank structure and regularization into modeling the sparse connectivity patterns reduces model complexity. Together, these efforts not only allow for the accurate localization and correction of site effects but also improve the interpretability of these effects in multi-site connectivity data.

The rest of this paper is organized as follows. In Section 2, we introduce SLACC (sparse latent covariate-driven connectome) factorization, a low-rank sparse latent factor model, for decomposing and harmonizing multi-site functional connectivity matrices, along with a penalized Expectation-Maximization (EM) algorithm. In Section 3, we conduct extensive simulations to demonstrate SLACC’s ability to recover true parameters and underlying connectivity patterns. In Section 4, we apply our method to the resting-state fMRI data from the Autism Brain Imaging Data Exchange (ABIDE) study and compare its performance with other harmonization approaches. We conclude with a discussion of the merits of SLACC, its limitations and future extensions in Section 5.

2 Methods

2.1 Notation and setup

In this paper, we formulate and present our model under a multi-site setting for generality, although a single-site setting can be considered as a special case if site effect correction is not a primary objective. Let $i = 1, \dots, M$ denote the site index and $j = 1, \dots, n_i$ denote the subject index in the i th site. We denote by $n = \sum_{i=1}^M n_i$ the total number of subjects in the study. Let \mathbf{x}_{ij} be the q -dimensional covariate vector for the subject j in the site i (e.g., age and sex), $\mathbf{X}_i \in \mathbb{R}^{n_i \times q}$ to be the \mathbf{x}_{ij} stacked in rows for the i th site, and $\mathbf{X} \in \mathbb{R}^{n \times q}$ be the \mathbf{X}_i stacked in rows across sites. Let \mathbf{Y}_{ij} be a $V \times V$ brain connectivity matrix for the subject j in the site i , where V denotes the number of brain regions. We define $\mathbf{y}_{ij} = \mathcal{T}(\mathbf{Y}_{ij})$ to be the vector of $p = V(V + 1)/2$ upper-triangular entries of \mathbf{Y}_{ij} including the diagonal entries, and is defined similarly for any symmetric matrix as an input.

In this paper, matrices are denoted by bold uppercase letters, while vectors are denoted by bold lowercase letters. $\mathbf{A} \odot \mathbf{B}$, refers to the Hadamard product of \mathbf{A} and \mathbf{B} in same dimension, \otimes denotes the Kronecker product, and $\mathbf{a} \circ \mathbf{b}$ refers to the outer product of \mathbf{a} and \mathbf{b} . $\text{diag}(\mathbf{a})$ refers to the diagonal matrix with entries \mathbf{a} . $\|\mathbf{a}\|_q$ refers to the L_q norm of \mathbf{a} .

2.2 Model

In our proposed model, \mathbf{Y}_{ij} is decomposed into a linear combination of symmetric rank-1 sparse connectivity patterns $\{\mathbf{u}_l \mathbf{u}_l^\top\}_{l=1}^L$ common to all sites, weighted by covariate-dependent subject scores $\{a_{ijl}\}_{l=1}^L$ that we further parameterize to capture site and covariate effects. These a_{ijl} terms enable our model to identify and correct for localized site-specific heterogeneity within and across brain functional networks, while also accounting for biological covariate effects.

Specifically, we assume that connectivity matrices \mathbf{Y}_{ij} follow the model:

$$\mathbf{Y}_{ij} = \sum_{l=1}^L a_{ijl} \times \mathbf{u}_l \mathbf{u}_l^\top + \mathbf{E}_{ij}. \quad (1)$$

Here, each $\mathbf{u}_l = (u_{l1}, \dots, u_{lV})^\top \in \mathbb{R}^V$ represents a vector of region weights for the l th sparsity pattern, and L represents the number of sparse connectivity patterns. Each element of the noise matrix \mathbf{E}_{ij} follows a Gaussian distribution:

$$\mathbf{E}_{ij}[v, v'] \stackrel{i.i.d.}{\sim} \mathcal{N}(0, \phi_i^2), \quad 1 \leq v \leq v' \leq V.$$

Note that Equation (1) is a common signal-plus-noise model to decompose and factorize brain connectivity, a specification widely used in the fMRI literature (Eavani et al., 2015; Zhao et al., 2021; Y. Wang & Guo, 2023), and the rank-1 patterns $\mathbf{u}_l \mathbf{u}_l^\top$ are well-informed by the observation that FC patterns often exhibit block-diagonal structure, as illustrated in Figure 1.

We further assume a linear model for a_{ijl} to incorporate covariate effects and site-related het-

erogeneity:

$$a_{ijl} = \mathbf{x}_{ij}^\top \boldsymbol{\beta}_l + \delta_{ijl}, \quad (2)$$

where $\delta_{ijl} \stackrel{i.i.d.}{\sim} \mathcal{N}(0, \sigma_{il}^2)$ for $j = 1, \dots, n_i$. To complete the model, we assume that \mathbf{E}_{ij} is independent of δ_{ijl} for all i, j, l .

We note that, in Equations (1) and (2), the site effects are characterized by three sources: site-specific mean effects (via $\mathbf{x}_{ij}^\top \boldsymbol{\beta}_l$), site-specific latent-factor variances (σ_{il}^2), and site-specific noise variance (ϕ_i^2), providing flexibility in capturing site-specific heterogeneity in mean and covariance.

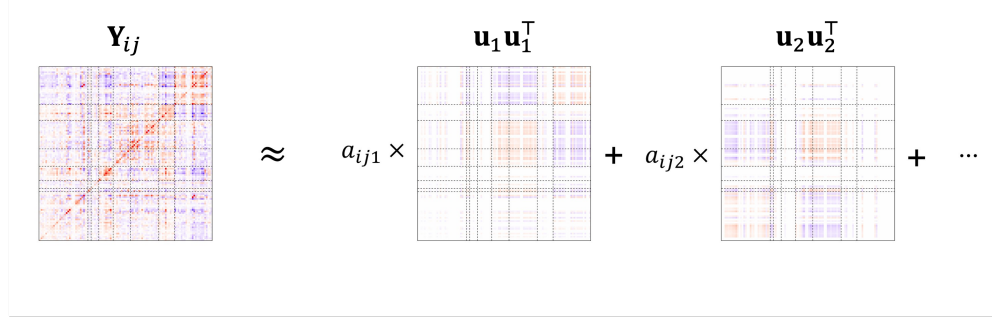


Figure 1: Illustration of framework decomposing a subject's connectivity matrix into sparse rank-1 connectivity patterns $\{\mathbf{u}_l \mathbf{u}_l^\top\}_{l=1}^L$, weighted by subject scores a_{ijl} modeled by covariates \mathbf{x}_{ij} .

2.3 Likelihood

Under (1)–(2), \mathbf{Y}_{ij} follows a multilinear normal model (Ohlson et al., 2013). Given the symmetry of \mathbf{Y}_{ij} , we derive its likelihood by considering the likelihood of $\mathbf{y}_{ij} = \mathcal{T}(\mathbf{Y}_{ij})$. For notational simplicity, define $\mathbf{s}_l = \mathcal{T}(\mathbf{u}_l \mathbf{u}_l^\top) \in \mathbb{R}^p$, $\mathbf{S} = [\mathbf{s}_1; \dots; \mathbf{s}_L] \in \mathbb{R}^{p \times L}$, and denote the regression coefficients as $\mathbf{B} = [\boldsymbol{\beta}_1; \dots; \boldsymbol{\beta}_L] \in \mathbb{R}^{q \times L}$.

Let $\boldsymbol{\Theta} = \{\mathbf{B}, \mathbf{U}, \sigma_{il}^2, \phi_i^2; i = 1, \dots, M, l = 1, \dots, L\}$ be the parameter set. Then \mathbf{y}_{ij} follows a multivariate normal distribution with mean

$$\boldsymbol{\mu}_{ij} = \mathbb{E}(\mathbf{y}_{ij} | \mathbf{x}_{ij}) = \sum_{l=1}^L (\mathbf{x}_{ij}^\top \boldsymbol{\beta}_l) \mathbf{s}_l = \mathbf{S} \mathbf{B}^\top \mathbf{x}_{ij},$$

and site-specific covariance

$$\boldsymbol{\Sigma}_i = \text{Cov}(\mathbf{y}_{ij} | \mathbf{x}_{ij}) = \sum_{l=1}^L \sigma_{il}^2 \mathbf{s}_l \mathbf{s}_l^\top + \phi_i^2 \mathbf{I}_p = \mathbf{S} \text{diag}(\sigma_{i1}^2, \dots, \sigma_{iL}^2) \mathbf{S}^\top + \phi_i^2 \mathbf{I}_p,$$

where \mathbf{I}_p is a $p \times p$ identity matrix. Then, the negative log-likelihood can then be written as

$$-\log \mathcal{L}(\boldsymbol{\Theta} | \mathbf{y}_{ij}) = \frac{1}{2} \log(2\pi) + \frac{1}{pn} \left\{ \sum_{i=1}^M \frac{n_i}{2} \log |\boldsymbol{\Sigma}_i| + \sum_{i=1}^M \sum_{j=1}^{n_i} \frac{1}{2} (\mathbf{y}_{ij} - \boldsymbol{\mu}_{ij})^\top \boldsymbol{\Sigma}_i^{-1} (\mathbf{y}_{ij} - \boldsymbol{\mu}_{ij}) \right\}. \quad (3)$$

2.4 Identifiability

Let \mathbb{Y} and \mathbb{E} denote the $n \times V \times V$ tensors that are formed by stacking \mathbf{Y}_{ij} and \mathbf{E}_{ij} with the first mode corresponding to subjects, and the second and third modes corresponding to regions. Then, our model is reformulated as a 3-way array model using CANDECOMP/PARAFAC (CP) decomposition:

$$\mathbb{Y} = \sum_{l=1}^L \mathbf{a}_l \circ \mathbf{u}_l \circ \mathbf{u}_l + \mathbb{E}, \quad \mathbf{a}_l = \mathbf{X}\boldsymbol{\beta}_l + \boldsymbol{\delta}_l, \quad (4)$$

where $\boldsymbol{\delta}_l = (\delta_{11l}, \dots, \delta_{1n_1l}, \dots, \delta_{M1l}, \dots, \delta_{Mn_Ml})^\top$. Under the CP decomposed form, we obtain the following result that equivalence of the likelihood implies equivalence of the parameters. The proof naturally follows the result of Lock & Li (2018).

Theorem 1 *The parameter set Θ is identifiable under the following regularity conditions:*

- A.1 $\min(n, q, L) \geq 2$ and $L < V$.
- A.2 $\mathbf{U} = [\mathbf{u}_1; \dots; \mathbf{u}_L]$ is of full column rank, and $\|\mathbf{u}_l\|_2 = 1$ for $l = 1, \dots, L$.
- A.3 The first nonzero entries of \mathbf{u}_l for $l = 1, \dots, L$ are positive.
- A.4 $\sigma_{11}^2 \geq \sigma_{12}^2 \geq \dots \geq \sigma_{1L}^2 > 0$.
- A.5 \mathbf{X} is of full column rank.

A.1 is needed to meet Kruskal's uniqueness condition that is required to establish identifiability, and A.2-A.4 are needed because CP decomposition is not identifiable under scaling, sign flipping, and re-ordering.

2.5 Parameter estimation

It should be noted in Section 2.2 that the objective function in (3) is not convex with respect to all parameters, making optimization challenging. More importantly, the sparsity of \mathbf{u}_l needs to be included into the optimization process. We develop a penalized EM algorithm for optimizing the conditional expectation of the log-likelihood (3) for fixed L . Choosing L is discussed in Section 2.7.

2.5.1 E-step

As $\mathbf{a}_{ij} \equiv (a_{ij1}, \dots, a_{ijL})^\top$ are latent variables in our model, the E-step updates \mathbf{a}_{ij} by computing its conditional expectation given the data \mathbf{y}_{ij} and the parameter estimates from the previous step:

$$E(\mathbf{a}_{ij} | \mathbf{y}_{ij}) = \boldsymbol{\Sigma}_{\mathbf{a}_{ij} | \mathbf{y}_{ij}} (\boldsymbol{\Sigma}_{\mathbf{a}_{ij}}^{-1} (\mathbf{B}^\top \mathbf{x}_{ij}) + \mathbf{S}^\top \boldsymbol{\Sigma}_{\mathbf{y}_{ij} | \mathbf{a}_{ij}}^{-1} \mathbf{y}_{ij}), \quad (5)$$

where $\boldsymbol{\Sigma}_{\mathbf{a}_{ij}} = \text{diag}(\sigma_{i1}^2, \dots, \sigma_{iL}^2)$, $\boldsymbol{\Sigma}_{\mathbf{y}_{ij} | \mathbf{a}_{ij}} = \phi_i^2 \cdot \mathbf{I}_p$, and $\boldsymbol{\Sigma}_{\mathbf{a}_{ij} | \mathbf{y}_{ij}} = \mathbf{S}^\top \boldsymbol{\Sigma}_{\mathbf{y}_{ij} | \mathbf{a}_{ij}}^{-1} \mathbf{S} + \boldsymbol{\Sigma}_{\mathbf{a}_{ij}}^{-1}$.

2.5.2 M-step: Updating $\boldsymbol{\beta}_l$, σ_{il}^2 , and ϕ_i^2

In the M-step, we maximize the conditional expectation of the joint log-likelihood of \mathbf{a}_{ij} and \mathbf{y}_{ij} . Since the joint log-likelihood of \mathbf{y}_{ij} and \mathbf{a}_{ij} can be decomposed into the log-likelihood of \mathbf{a}_{ij} and the

conditional log-likelihood of \mathbf{y}_{ij} given \mathbf{a}_{ij} , the M-step is partitioned into two optimization problems:

$$\max_{\{\beta_l\}_{l=1}^L, \{\sigma_{il}^2\}_{i=1, l=1}^{M, L}} \sum_{i=1}^M \sum_{j=1}^{n_i} \mathbb{E}_{\mathbf{a}_{ij}|\mathbf{y}_{ij}} [\log \mathcal{L}(\mathbf{a}_{ij})] \quad \text{and} \quad \max_{\{\mathbf{u}_l\}_{l=1}^L, \{\phi_i^2\}_{i=1}^M} \sum_{i=1}^M \sum_{j=1}^{n_i} \mathbb{E}_{\mathbf{a}_{ij}|\mathbf{y}_{ij}} [\log \mathcal{L}(\mathbf{y}_{ij}|\mathbf{a}_{ij})]. \quad (6)$$

where $\mathbb{E}_{\mathbf{a}_{ij}|\mathbf{y}_{ij}}$ represents the conditional expectation of \mathbf{a}_{ij} given \mathbf{y}_{ij} . For parameters $\{\beta_l, \sigma_{il}^2, \phi_i^2\}$, the closed-form solutions can be derived during each M-step. However, updating \mathbf{u}_l requires additional algorithmic procedure that we address in Section 2.5.3. The first optimization problem in Equation (6) can be further separated into two parts, one updating β_l and the other updating σ_{il}^2 .

Updating β_l . The part of the expected complete-data log-likelihood that depends on β_l is

$$Q(\beta_l) = -\frac{1}{2} \sum_{i=1}^M \sum_{j=1}^{n_i} \frac{(a_{ijl} - \mathbf{x}_{ij}^\top \beta_l)^2}{\sigma_{il}^2} + \text{constant},$$

which is reduced to the weighted least squares problem, yielding the closed form as follows:

$$\hat{\beta}_l = \left(\sum_{i=1}^M \sum_{j=1}^{n_i} \frac{\mathbf{x}_{ij} \mathbf{x}_{ij}^\top}{\sigma_{il}^2} \right)^{-1} \left(\sum_{i=1}^M \sum_{j=1}^{n_i} \frac{\mathbf{x}_{ij} a_{ijl}}{\sigma_{il}^2} \right). \quad (7)$$

Updating σ_{il}^2 . The site-specific conditional second-moment estimator is provided by

$$\frac{1}{n_i} \sum_{j=1}^{n_i} ((\mathbf{a}_{ij} - \mathbf{B}^\top \mathbf{x}_{ij})(\mathbf{a}_{ij} - \mathbf{B}^\top \mathbf{x}_{ij})^\top + \Sigma_{\mathbf{a}_{ij}|\mathbf{y}_{ij}}). \quad (8)$$

From here, $\{\sigma_{il}^2\}_{i=1}^M$ is obtained by taking diagonal entries of the above form.

Updating ϕ_i^2 . ϕ_i^2 is updated by

$$\begin{aligned} \hat{\phi}_i^2 &= \frac{1}{n_i p} \sum_{j=1}^{n_i} \mathbb{E}_{\mathbf{a}_{ij}|\mathbf{y}_{ij}} \|\mathbf{y}_{ij} - \mathbf{S}\mathbf{a}_{ij}\|_2^2 \\ &= \frac{1}{n_i p} \sum_{j=1}^{n_i} \|\mathbf{y}_{ij} - \mathbf{S}\mathbf{a}_{ij}\|_2^2 + \frac{1}{p} \text{tr}(\mathbf{S} \Sigma_{\mathbf{a}_{ij}|\mathbf{y}_{ij}} \mathbf{S}^\top). \end{aligned} \quad (9)$$

2.5.3 M-step: updating \mathbf{u}_l with regularization

Provided parameter updates in Sections 2.5.1 and 2.5.2, the M-step for updating $\mathbf{U} \equiv [\mathbf{u}_1; \dots; \mathbf{u}_L]$ without any penalization is equivalent to

$$\mathbf{U} = \operatorname{argmin}_{\mathbf{U}} \sum_{i=1}^M \sum_{j=1}^{n_i} \frac{\|\mathbf{Y}_{ij} - \mathbf{U}\Pi_{ij}\mathbf{U}^\top\|_F^2 + \operatorname{tr}((\mathbf{U}^\top \mathbf{U} \odot \mathbf{U}^\top \mathbf{U}) \Sigma_{\mathbf{a}_{ij}|\mathbf{y}_{ij}})}{4\phi_i^2}, \quad (10)$$

where $\Pi_{ij}^{(t)} = \operatorname{diag}(a_{ij1}, \dots, a_{ijL}) \in \mathbb{R}^{L \times L}$. Its derivation is presented in Supplementary material A. To achieve sparsity, we propose to use L_0 regularization on \mathbf{U} s for two reasons. First, it provides estimates with less bias compared to other regularization methods (e.g., Lasso and ridge penalties), while still ensuring sparsity. This step is critical for harmonization, as it allows for more accurate identification and correction of site effects. Second, L_0 regularization enables us to incorporate the Bayesian Information Criterion (BIC) directly into the M-step, thus avoiding the need for computationally expensive fine-tuning of parameters.

Specifically, when all the parameters other than \mathbf{U} are fixed, the penalized objective guided by BIC is:

$$\widehat{\mathbf{U}} = \operatorname{argmin}_{\mathbf{U}} \sum_{i=1}^M \sum_{j=1}^{n_i} \frac{\|\mathbf{Y}_{ij} - \mathbf{U}\Pi_{ij}\mathbf{U}^\top\|_F^2 + \operatorname{tr}((\mathbf{U}^\top \mathbf{U} \odot \mathbf{U}^\top \mathbf{U}) \Sigma_{\mathbf{a}_{ij}|\mathbf{y}_{ij}})}{2\phi_i^2} + \log(n) \cdot \|\mathbf{U}\|_0. \quad (11)$$

Solving Equation (11) poses two computational challenges regarding non-convexity. First, directly optimizing over L_0 penalty is computationally intractable. To mitigate this issue, we consider the Truncated Lasso Penalty (TLP), a surrogate of L_0 penalty expressed by $\|\mathbf{U}\|_0 \approx \sum_{v=1}^V \sum_{l=1}^L \min\left(\frac{|u_{vl}|}{\tau}, 1\right)$ (Shen et al., 2012). Here, $\tau > 0$ is a tuning parameter controlling the degree of approximation, and the τ value closer to 0 makes TLP close to the L_0 penalty. Following the default implementation of Shen et al. (2012) where the default τ depends on the dimensionality, we choose $\tau = 0.5 \cdot \sqrt{\log(VL)/n}$ as a default. Second, even the (unpenalized) objective in \mathbf{U} contains bilinear form $\mathbf{U}\Pi_{ij}\mathbf{U}^\top$, making Equation (11) computationally challenging. We handle this by using the Alternating Direction Method of Multipliers (ADMM) splitting, which allows mitigating the non-convexity by alternating convex subproblems. Specifically, we introduce an auxiliary copy \mathbf{U}^* of \mathbf{U} and enforce the consensus constraints $\mathbf{U} = \mathbf{U}^*$.

Addressing the proposed solutions to the challenges above results in the updated objective

$$\begin{aligned} \widehat{\mathbf{U}} = \operatorname{argmin}_{\mathbf{U}} & \sum_{i=1}^M \sum_{j=1}^{n_i} \frac{\|\mathbf{Y}_{ij} - \mathbf{U}^*\Pi_{ij}\mathbf{U}^\top\|_F^2 + \operatorname{tr}((\mathbf{U}^{*\top} \mathbf{U} \odot \mathbf{U}^{*\top} \mathbf{U}) \Sigma_{\mathbf{a}_{ij}|\mathbf{y}_{ij}})}{2\phi_i^2} \\ & + \frac{\log(n)}{2} \sum_{v=1}^V \sum_{l=1}^L \frac{I(|u_{vl}| \leq \tau)}{\tau} |u_{vl}| + \frac{\log(n)}{2} \sum_{v=1}^V \sum_{l=1}^L \frac{I(|u_{vl}^*| \leq \tau)}{\tau} |u_{vl}^*|, \end{aligned} \quad (12)$$

subject to the $\mathbf{U} = \mathbf{U}^*$ that we solve using ADMM by alternating updates of \mathbf{U} and \mathbf{U}^* under the consensus constraint $\mathbf{U} = \mathbf{U}^*$. Analogous to the one-step update done in Shen et al. (2012),

we replace $u_{v,l}$ and $u_{v,l}^*$ in the penalty term with the estimates from the previous step of the EM algorithm, i.e., $u_{v,l}^{(t-1)}$ and $u_{v,l}^{*,(t-1)}$. The details are illustrated in Supplementary material B.

2.6 Algorithmic considerations

Altogether, our algorithm when L is fixed is summarized in Algorithm 1.

Algorithm 1 Penalized EM algorithm, when L is provided

- 1: **Initialize:** Initialize $\mathbf{U}^{(0)}$, $\mathbf{a}_{ij}^{(0)}$, $\mathbf{B}^{(0)}$, $\sigma_{il}^{2(0)}$ and $\phi_i^{2(0)}$.
- 2: **for** $t = 1, 2, \dots$ until convergence **do**
- 3: **E-step:** Given $\mathbf{U}^{(t-1)}$, $\mathbf{B}^{(t-1)}$, $\sigma_{il}^{2(t-1)}$, and $\phi_i^{2(t-1)}$, update $\mathbf{a}_{ij}^{(t)}$ using Equation (5).
- 4: **M-step:** Given $\mathbf{a}_{ij}^{(t)}$, $\phi_i^{2(t-1)}$, and $\mathbf{U}^{(t-1)}$ update $\mathbf{U}^{(t)}$ by solving Equation (12).
- 5: **M-step:** Given $\mathbf{a}_{ij}^{(t)}$, $\mathbf{U}^{(t)}$, $\sigma_{il}^{2(t-1)}$ and $\phi_i^{2(t-1)}$ update $\mathbf{B}^{(t)}$ and $\sigma_{il}^{2(t)}$, using Equations (7) and (8).
- 6: **M-step:** Given $\mathbf{a}_{ij}^{(t)}$, $\mathbf{U}^{(t)}$, $\phi_i^{2(t-1)}$ and $\sigma_{il}^{2(t)}$, update $\phi_i^{2(t)}$ using Equation (9).
- 7: **Check for convergence:** If $\|\mathbf{U}^{(t)} - \mathbf{U}^{(t-1)}\|_F < \epsilon$, stop the algorithm.
- 8: **end for**
- 9: **Normalize:** Normalize $\mathbf{u}_l^{(t)}$ with $\|\mathbf{u}_l^{(t)}\|_2 = 1$ and make corresponding adjustments to \mathbf{B} and σ_{il}^2 .
- 10: **Return:** $\widehat{\Theta} = \{\mathbf{U}^{(t)}, \mathbf{B}^{(t)}, \sigma_{il}^{2(t)}, \phi_i^{2(t)}\}$

We note that each step of updating \mathbf{U} in the penalized EM could lead to a local minimum, especially when L is high. To improve algorithmic stability, we find that implementing the unpenalized EM (i.e., solving Equation (10)) initialized with higher-order singular value decomposition (De Lathauwer et al., 2000) and using the estimates as the initial estimates of the penalized EM algorithm significantly improves the convergence behavior. In addition to this, we find that an annealing strategy that gradually increases the penalty in Equation (12) from 0 (unpenalized EM) to $\log(n)$ at each iteration of the EM further mitigates the local minimum problem.

2.7 Selection of L

Up to this point, we have assumed that L in our model is known. To choose L from the data, we use the extended BIC to choose L (J. Chen & Chen, 2008). Specifically, the extended BIC is defined as:

$$\text{EBIC}(\widehat{\Theta}) = -2 \sum_{i=1}^M \sum_{j=1}^{n_i} \log \mathcal{L}(\widehat{\Theta} | \mathbf{y}_{ij}) + \log(n) \cdot \text{df}(\widehat{\Theta}) + 2\gamma \log(p) \cdot \text{df}(\widehat{\Theta}), \quad (13)$$

where $\text{df}(\widehat{\Theta}) = qL + ML + M + \|\widehat{\mathbf{U}}\|_0$, the number of nonzero elements of the parameter set. $0 \leq \gamma \leq 1$ is chosen by user, and we set $\gamma = 0.5$ as a default. If p is deemed to be high, higher values of up to $\gamma = 1$ can be used. Alternative strategies may be used, such as site-stratified likelihood cross-validation to measure bias-variance tradeoff.

2.8 Harmonization

After estimating parameters, we construct the harmonized data by removing site-specific means, normalizing site-specific variances for each latent factor, and rescaling the residual variances. Note that, if \mathbf{x}_{ij} includes biological covariates \mathbf{z}_{ij} and site dummy variables, then $\mathbf{x}_{ij}^\top \boldsymbol{\beta}_l$ can be rewritten as $\alpha_l + \mathbf{z}_{ij}^\top \boldsymbol{\theta}_l + \gamma_{il}$ with the constraint $\sum_{i=1}^M \gamma_{il} = 0$. Since the site-specific heterogeneity is embedded in both the latent factors and the residual noise, we harmonize them as

$$a_{ijl}^{(h)} = \frac{\sigma_l^{(h)}}{\hat{\sigma}_{il}} (\hat{a}_{ijl} - \hat{\alpha}_l - \mathbf{z}_{ij}^\top \hat{\boldsymbol{\theta}}_l - \hat{\gamma}_{il}) + \hat{\alpha}_l + \mathbf{z}_{ij}^\top \hat{\boldsymbol{\theta}}_l, \quad \mathbf{E}_{ij}^{(h)} = \frac{\phi^{(h)}}{\hat{\phi}_i} \hat{\mathbf{E}}_{ij}, \quad (14)$$

where $\sigma_l^{(h)} = \sqrt{\frac{\sum_{i=1}^M n_i \hat{\sigma}_{il}^2}{n}}$, $\phi^{(h)} = \sqrt{\frac{\sum_{i=1}^M n_i \hat{\phi}_i^2}{n}}$. The harmonized data is therefore given by

$$\mathbf{Y}_{ij}^{(h)} = \sum_{l=1}^L a_{ijl}^{(h)} \hat{\mathbf{u}}_l \hat{\mathbf{u}}_l^\top + \mathbf{E}_{ij}^{(h)}.$$

3 Simulation studies

In this section, we evaluate the performance of our model through two simulation studies designed to validate theoretical properties, assess robustness, and demonstrate practical utility.

3.1 Simulation 1

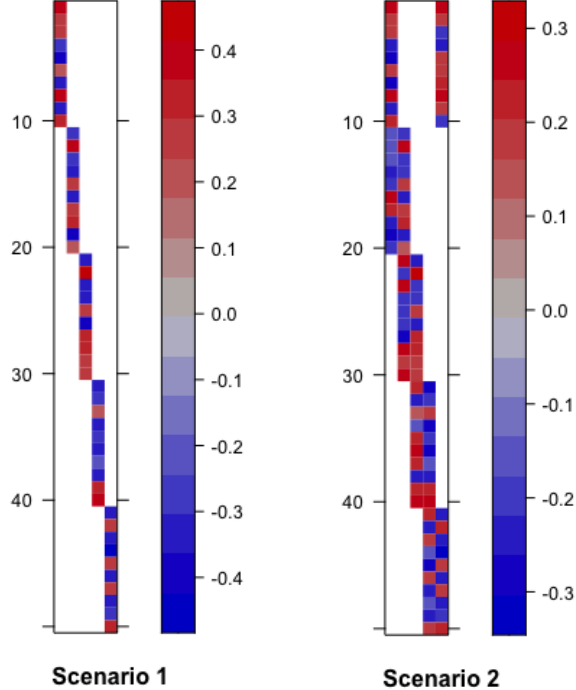


Figure 2: True $\mathbf{U} \in \mathbb{R}^{50 \times 5}$ for scenarios 1 and 2 used in simulation studies.

Simulation 1 evaluates parameter estimation under varying sample sizes ($n = 100, 200, \dots, 500$), when true L is specified correctly. We specify $M = 2, L = 5, V = 50$ ($p = 1275$), and $q = 4$. We considered two possible scenarios of \mathbf{U} as illustrated in Figure 4: (i) Scenario 1 is the case where there are no overlapping entries across V and 20% of the entries are nonzero, and scenario 2 has overlapping elements and 40% of the entries are nonzero. Each nonzero entries for both scenarios were generated once from $\text{Uniform}(0.5, 1.0)$ and multiplied by either 1 or -1 randomly, then each column of \mathbf{U} was normalized to have unit norm. We used 4 covariates in total, consisting of two continuous biological covariates and two site-specific intercepts. The biological covariates were generated from $\mathcal{N}(0, 1)$ and the corresponding regression coefficients were also generated from $\mathcal{N}(0, 1)$ and kept fixed throughout the simulation. Site-specific intercepts for each l were fixed to be 0.3 for site 1 and -0.3 for site 2 for every $l = 1, \dots, 5$. For variance components, we set $\sigma_{11}^2 = 1, \sigma_{11}^2 = 2, \dots, \sigma_{15}^2 = 5$ for site 1 and $\sigma_{21}^2 = 5, \sigma_{22}^2 = 4, \dots, \sigma_{25}^2 = 1$ for site 2. Lastly, we set $\phi_1^2 = 1.2$ and $\phi_2^2 = 0.8$. It yielded the median of σ^2 parameters divided by the median of ϕ^2 parameters equal to 3, and we note that it is considerably lower than the fit from the real data analysis in Section 4 in which the ratio was nearly 25.

For each sample size, we repeated the simulation $B = 1000$ times. After fitting the model, the column order as the sign of $\widehat{\mathbf{U}}$ were reordered based on the correlation between $\widehat{\mathbf{U}}$ and \mathbf{U} , and other parameters were re-ordered accordingly.

Due to the lack of statistical methods addressing the same problem, we considered two related methods as competitors: (i) **(SLACC-True)** SLACC with true \mathbf{U} provided, which serves as a benchmark, and (ii) **(SLACC-NoPen)** SLACC without penalization in the M-step in updating \mathbf{U} . To compare the performances, we use the following metrics. We first compare mean square error (MSE) for $\mathbf{B}, \{\sigma_{il}^2\}_{i=1, l=1}^{2, 5}, \{\phi_i^2\}_{i=1}^2$. For example, the MSE for $\widehat{\mathbf{U}}$ is computed by $1/B \cdot \sum_{b=1}^B \|\widehat{\mathbf{U}}^{(b)} - \mathbf{U}\|_F^2$ where $\widehat{\mathbf{U}}^{(b)}$ is the estimated \mathbf{U} from the b th simulation. The variance ($1/B \cdot \sum_{b=1}^B \|\widehat{\mathbf{U}}^{(b)} - \sum_{b=1}^B \mathbf{U}^{(b)}/B\|_F^2$) as well as bias² (defined as MSE – variance) are reported. Second, we evaluated sensitivity and specificity of $\widehat{\mathbf{U}}$. Sensitivity is defined as the proportion that $\widehat{\mathbf{U}}^{(b)}$ captures the true nonzero indices out of the number of nonzero entries of \mathbf{U} , and specificity is defined as the proportion that $\widehat{\mathbf{U}}^{(b)}$ captures the true zero indices out of the number of zero entries of \mathbf{U} . Note that, trivially, the sensitivity and specificity of SLACC-True are both 100% and the values for SLACC-NoPen are 100% and 0% respectively.

Figure 3 shows the results in Simulation 1. The overall patterns look similar in both scenarios, and we see a clearly decreasing MSE as sample size increases bounded above the performance of SLACC-true in all parameters. SLACC achieved consistently lower MSE than SLACC-NoPen in estimating \mathbf{U} , while the difference in performance on other parameters become marginal as sample size increases. We also note that, attributed to the surrogate L_0 penalization, the bias in SLACC's parameter estimation was similar to SLACC-NoPen or often lower (e.g., in estimating ϕ_i^2). Also, the surrogate L_0 penalty in estimating \mathbf{U} achieved high sensitivity and specificity in all n except for $n = 100$, which imply the case where the low signal-to-residual-noise (e.g., \mathbf{B} and σ_{il}^2 in relative to ϕ_i^2) impedes the estimation of \mathbf{U} .



Figure 3: Results of Simulation 1. The left and right columns describe scenarios 1 and 2, respectively. The first 4 rows describe MSE (red+blue), bias² (red) and variance (blue). The last row shows sensitivity and specificity of the estimated \mathbf{U} .

3.2 Simulation 2

Simulation 2 evaluates the EBIC approach in selecting the true $L = 5$ used in Simulation 1. We fit the model with varying L in the grid $L \in \{2, 3, \dots, 10\}$ and extracted EBIC for each fit. The results of estimated L over 200 simulations are reported in Figure 6 of Supplementary material C. As expected, as n increases, the distribution of the chosen L gets closer to the true L in both scenarios. Similar to the sensitivity/specificity results discussed in Simulation 1, the BIC criterion is shown to be conservative depending on the signal-to-residual-noise ratio or sample size. Compared to scenario 1 where \mathbf{u}_l were orthogonal and the nonzero indices were not overlapping, a higher n was needed to consistently recover the true L as shown in Scenario 2.

4 Data analysis

4.1 Data preparation and preprocessing

We use preprocessed resting-state fMRI (rs-fMRI) data from the Autism Brain Imaging Data Exchange (ABIDE) (Di Martino et al., 2014) to empirically evaluate our model’s performance. ABIDE is a multi-site consortium providing rs-fMRI data from 408 subjects with Autism Spectrum Disorder (ASD) and 476 controls. Due to the lack of prior coordination between sites, scan parameters, scanner types, and diagnostic/assessment protocols varied across sites. The sample size for each site ranged from 21 (CALTECH) to 169 (NYU). In addition to the existing evidence of site effects on functional connectivity (Yu et al., 2018), we also note that the number of scans per person varied substantially by sites, ranging from 78 (OHSU) to 296 time points (UM), which serves as a design-based evidence of site effects in variances because FC is a statistical estimate whose variance depends on the number of time points.

We used the ABIDE dataset preprocessed using the Configurable Pipeline for the Analysis of Connectomes (CPAC), which includes slice-timing correction, motion realignment, and intensity normalization. Further preprocessing details are provided in Craddock et al. (2013). The fMRI time-series for a set of regions of interest (ROIs) were obtained from the Harvard-Oxford (HO) atlas (Desikan et al., 2006; Frazier et al., 2005), which consists of $V = 110$ ROIs that we subsequently map to Yeo’s 7-network parcellation (Yeo et al., 2011) plus the subcortical network. The resulting 8 functional networks include the Visual Network (VN), Subcortical Network (Scor), Somatomotor Network (SMN), Salience/Ventral Attention Network (SN/VAN), Limbic Network (LN), Fron-toparietal Control Network (FPCN), Dorsal Attention Network (DAN) and Default Mode Network (DMN).

We excluded 38 subjects with incomplete brain coverage and the CMU site due to its limited sample size (5 subjects). The final sample comprises 845 subjects across 16 sites. We then computed Fisher-transformed Pearson correlation matrices from the fMRI time-series data. Since our goal is to understand the individual differences in connectivity, we removed the sample mean across subjects for each edge as a preprocessing step. The diagonal entries were set to 0 and were not used in estimating ϕ_i^2 .

4.2 Results

We included six biological covariates in all methods: age, age^2 , sex, diagnosis, $age \times sex$, and $age \times diagnosis$. We split the data into two folds consisting of 591 (70%) training and 254 (30%) test subjects, stratified by each study site. We fit our model to the training data, with $L = 73$ selected by EBIC. About 68.2% of the entries in $\widehat{\mathbf{U}}$ were 0, which is shown in Figure 4. Our analysis reveals that the covariate-dependent latent patterns seem to vary across within-network and between-network structures. For example, a subset of regions in visual network (VN) had a noticeable similarity in latent patterns, and these seemed to be related to the salience/ventral attention network (SN/VAN) as well as frontoparietal control network (FPCN). At the same time, some latent patterns are very sparse and concentrated on a very few regions not clearly aligned with network structure.

We used the estimated parameters to extract the latent subject scores \hat{a}_{ijl} for both the training and test data. Then, using the estimated parameters, we further constructed the ‘batch-free’ model with the parameters $\{\hat{\mathbf{u}}_l, \hat{\boldsymbol{\theta}}_l, \hat{\alpha}_l, \sigma_l^{(h)} \phi^{(h)}\}_{l=1}^L$ defined in Section 2.8, and obtained the corrected latent subject scores, denoted by \hat{a}_{ijl}^* , for both training and test data. We calculated two F test statistics for each edge to test (i) equality in means across sites and (ii) equality of variance across sites using absolute residuals as in Levene’s test (Carroll & Schneider, 1985).

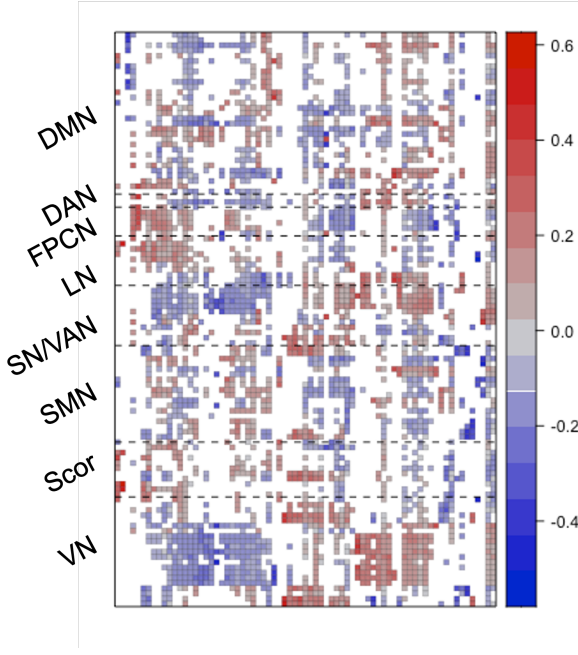


Figure 4: Estimated \mathbf{U} ($L = 73$) using the training data ($n = 591$), with the column orders obtained by hierarchical clustering.

As seen in Figure 5, SLACC identified latent factors in training data that are highly associated with site effects in means and variances, and a few of them exhibited huge effects (i.e., $F > 10$ in training data). After harmonization, most statistics shrink toward the null level. Although the average F statistic lower than 1 (expected value of the F distribution under the null) may occur

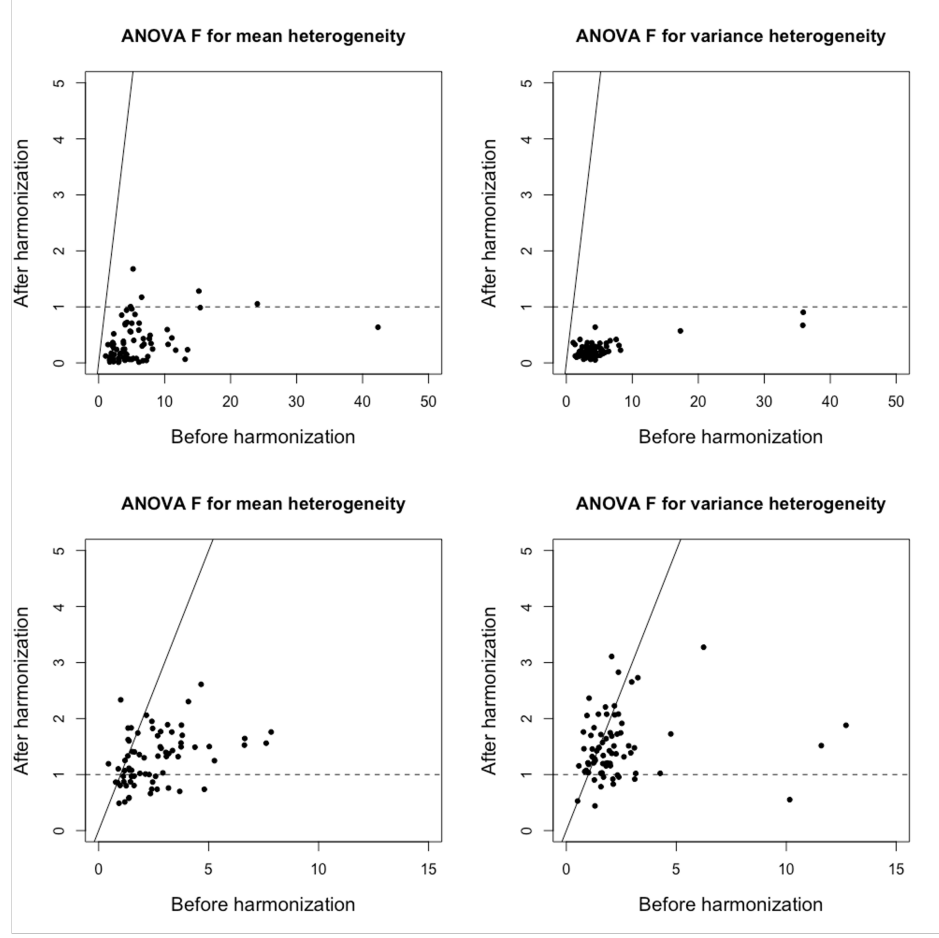


Figure 5: F test statistic for measuring mean and variance heterogeneity across sites, using both training (first row) and test data (second row). The dotted horizontal line is the expected value of the null F distribution (i.e., no site effects). The solid line is the 45 degree line.

due to overfitting to the training data, our results on the test data also show that most F statistics are reduced closer to the nominal level as well, which is more evident for the latent features with large F statistics before harmonization.

We further compared the edge-level harmonization performance of SLACC to ComBat (Fortin et al., 2018), which adjusts feature-wise means and variances using a normal-inverse-gamma prior and uses Empirical Bayes for estimation. For ComBat, we used `ComBatFamily` (<https://github.com/andy1764/ComBatFamily>, ver. 0.2.1) to fit the model on the training data and to harmonize the test data. On the edge level, the median F for mean and variance were 1.40 and 1.08 for SLACC, compared to 1.25 and 1.15 for ComBat. This suggests that SLACC more effectively harmonizes variances, whereas ComBat more effectively harmonizes means. Lastly, we evaluate how well our method preserves biological variations. For each harmonized test data, we extracted p values for each edge by using the six covariates. ComBat had 7.58% of the p values less than 0.05, and SLACC had 7.40%. While ComBat was slightly more effective in preserving biological variations, we also note that biological covariates including age and sex were correlated with sites in the ABIDE data,

which might have confounded in the harmonization step (Bridgeford et al., 2025).

5 Discussion

In this paper, we propose SLACC, a novel statistical method for decomposing brain connectivity data into sparse rank-1 latent patterns and covariate-dependent subject scores in both mean and variance. We studied the identifiability of the model parameters under mild regulatory conditions and proposed a surrogate L_0 penalized EM algorithm guided by the BIC, ensuring less biased parameter estimation while avoiding computationally expensive tuning. In our applications in a multi-site brain connectivity study, it enables modeling site effects in three different ways, improving interpretability and model-based understanding of site effects. By leveraging low-rank, sparse representations of connectivity matrices within the probabilistic modeling framework, SLACC captures and corrects artificial site effects through latent factors, preserving the underlying brain network structure. Incorporating low-rank structure and regularization reduces model complexity, leading to more reliable localization and correction of site effects.

Our work bridges recent advances in brain connectivity modeling for addressing popular ‘batch effects’ problems in neuroimaging. Recent work on blind source separation for brain connectivity (Y. Wang & Guo, 2023) models its sparse latent patterns while allowing each latent patterns have rank greater than 1. However, establishing identifiability and incorporating covariate effects in a generative model framework has been limited. A related approach aimed to adopt covariate-driven factorization of brain connectivity, but adopting sparsity of latent patterns in high dimension is non-trivial (Zhao et al., 2021; Park, 2025). By restricting latent patterns to be rank-1, our method achieves (i) identification of model parameters (ii) sparsity directly enforced in estimating \mathbf{u}_l s, and (iii) flexibility in modeling latent subject scores. Moreover, our model for latent subject scores is grounded in a linear modeling framework, which can be extended to more complex settings (e.g., longitudinal designs).

The proposed model has some room for extension. First, our assumption that connectivity data follow a multivariate normal distribution does not guarantee that the harmonized connectivity matrices are positive semidefinite, which is a statistical property in brain connectivity derived from fMRI BOLD time series in addition to symmetry considered in this paper. We note, however, that (i) most brain-wide association studies (BWASs) rely on univariate correlational analysis of edge-level connectivity and a behavioral outcome and do not explicitly utilize the positive semidefiniteness, and (ii) not all brain connectivity matrices are positive semidefinite (e.g., structural connectivity). For these reasons, we focused on a general setting that enforces symmetry and modeled structured relationships. When ensuring positive definiteness is important, a simple remedy would be to truncate negative eigenvalues to 0 after applying SLACC. Another direction is to incorporate alternative distributional assumptions (e.g., Wishart distributions) or log-link functions to model latent factors. Such adaptations, however, may compromise the computational efficiency (e.g., closed-form solutions in the estimation) and interpretability (e.g., mean/variance/covariance specification of site effects) offered by the current normal distribution framework. Second, SLACC

decomposes connectivity matrices into a set of rank-1 matrices of latent patterns, which may limit the method’s ability to recover neural circuits with complex topological structures or spatial patterns that extend beyond a rank-1 structure (Y. Wang & Guo, 2023). A potential extension of the SLACC framework could involve adopting more flexible higher-rank representations to better capture such complexity. Nevertheless, this extension would require addressing challenges such as ensuring identifiability. Third, uncertainty quantification and hypothesis testing for model parameters in latent subject scores is not straightforward, and it might require conditioning on \hat{u}_l s being known, as Zhao & Zhao (2025) also noted.

Software availability

The R package for implementing SLACC is publicly available at <https://github.com/junjypark/SLACC>.

Declaration of competing interests

None.

Acknowledgements

We would like to thank Dr. Piotr Zwiernik (University of Toronto) and Dr. Lindsay D. Oliver (Centre for Addiction and Mental Health) for their helpful suggestions.

Funding

RZ was partially supported by the University of Toronto’s Data Sciences Institute through the doctoral student fellowship. ET was partially supported by the Natural Sciences and Engineering Research Council of Canada under grant RGPIN-2023-04727, the University of Toronto Data Science Institute, and the University of Toronto McLaughlin Centre. JYP was partially supported by the Natural Sciences and Engineering Research Council of Canada under grant RGPIN-2022-04831, the University of Toronto Data Science Institute, and the Connaught Fund. The computing resources were enabled in part by support provided by University of Toronto and the Digital Research Alliance of Canada.

References

Biswal, B., Zerrin Yetkin, F., Haughton, V. M., & Hyde, J. S. (1995). Functional connectivity in the motor cortex of resting human brain using echo-planar MRI. *Magnetic Resonance in Medicine*, 34(4), 537–541.

Bridgeford, E. W., Powell, M., Kiar, G., Noble, S., Chung, J., Panda, S., ... others (2025). When no answer is better than a wrong answer: A causal perspective on batch effects. *Imaging Neuroscience*, 3, imag_a_00458.

Cai, B., Zille, P., Stephen, J. M., Wilson, T. W., Calhoun, V. D., & Wang, Y. P. (2017). Estimation of dynamic sparse connectivity patterns from resting state fMRI. *IEEE Transactions on Medical Imaging*, 37(5), 1224–1234.

Carroll, R. J., & Schneider, H. (1985). A note on Levene's tests for equality of variances. *Statistics & Probability Letters*, 3(4), 191–194.

Chen, A. A., Beer, J. C., Tustison, N. J., Cook, P. A., Shinohara, R. T., Shou, H., & Initiative, A. D. N. (2022). Mitigating site effects in covariance for machine learning in neuroimaging data. *Human Brain Mapping*, 43(4), 1179–1195.

Chen, A. A., Srinivasan, D., Pomponio, R., Fan, Y., Nasrallah, I. M., Resnick, S. M., ... others (2022). Harmonizing functional connectivity reduces scanner effects in community detection. *NeuroImage*, 256, 119198.

Chen, J., & Chen, Z. (2008). Extended bayesian information criteria for model selection with large model spaces. *Biometrika*, 95(3), 759–771.

Craddock, C., Sikka, S., Cheung, B., Khanuja, R., Ghosh, S. S., Yan, C., ... others (2013). Towards automated analysis of connectomes: The configurable pipeline for the analysis of connectomes (c-pac). *Frontiers in Neuroinformatics*, 42(10.3389).

De Lathauwer, L., De Moor, B., & Vandewalle, J. (2000). A multilinear singular value decomposition. *SIAM journal on Matrix Analysis and Applications*, 21(4), 1253–1278.

Desikan, R. S., Ségonne, F., Fischl, B., Quinn, B. T., Dickerson, B. C., Blacker, D., ... others (2006). An automated labeling system for subdividing the human cerebral cortex on MRI scans into gyral based regions of interest. *NeuroImage*, 31(3), 968–980.

Di Martino, A., Yan, C.-G., Li, Q., Denio, E., Castellanos, F. X., Alaerts, K., ... others (2014). The autism brain imaging data exchange: towards a large-scale evaluation of the intrinsic brain architecture in autism. *Molecular Psychiatry*, 19(6), 659–667.

Eavani, H., Satterthwaite, T. D., Filipovych, R., Gur, R. E., Gur, R. C., & Davatzikos, C. (2015). Identifying sparse connectivity patterns in the brain using resting-state fMRI. *NeuroImage*, 105, 286–299.

Fortin, J.-P., Cullen, N., Sheline, Y. I., Taylor, W. D., Aselcioglu, I., Cook, P. A., ... others (2018). Harmonization of cortical thickness measurements across scanners and sites. *NeuroImage*, 167, 104–120.

Fortin, J.-P., Parker, D., Tunç, B., Watanabe, T., Elliott, M. A., Ruparel, K., ... others (2017). Harmonization of multi-site diffusion tensor imaging data. *NeuroImage*, 161, 149–170.

Fox, M. D., & Greicius, M. (2010). Clinical applications of resting state functional connectivity. *Frontiers in Systems Neuroscience*, 4, 1443.

Fox, M. D., Snyder, A. Z., Vincent, J. L., Corbetta, M., Van Essen, D. C., & Raichle, M. E. (2005). The human brain is intrinsically organized into dynamic, anticorrelated functional networks. *Proceedings of the National Academy of Sciences*, 102(27), 9673–9678.

Frazier, J. A., Chiu, S., Breeze, J. L., Makris, N., Lange, N., Kennedy, D. N., ... others (2005). Structural brain magnetic resonance imaging of limbic and thalamic volumes in pediatric bipolar disorder. *American Journal of Psychiatry*, 162(7), 1256–1265.

Friston, K. J., Frith, C. D., Liddle, P. F., & Frackowiak, R. S. (1993). Functional connectivity: the principal-component analysis of large (PET) data sets. *Journal of Cerebral Blood Flow & Metabolism*, 13(1), 5–14.

Greicius, M. D., Krasnow, B., Reiss, A. L., & Menon, V. (2003). Functional connectivity in the resting brain: a network analysis of the default mode hypothesis. *Proceedings of the National Academy of Sciences*, 100(1), 253–258.

Johnson, W. E., Li, C., & Rabinovic, A. (2007). Adjusting batch effects in microarray expression data using empirical Bayes methods. *Biostatistics*, 8(1), 118–127.

Lock, E. F., & Li, G. (2018). Supervised multiway factorization. *Electronic Journal of Statistics*, 12(1), 1150.

Marrelec, G., Krainik, A., Duffau, H., Péligrini-Issac, M., Lehéricy, S., Doyon, J., & Benali, H. (2006). Partial correlation for functional brain interactivity investigation in functional MRI. *NeuroImage*, 32(1), 228–237.

Ohlson, M., Ahmad, M. R., & Von Rosen, D. (2013). The multilinear normal distribution: Introduction and some basic properties. *Journal of Multivariate Analysis*, 113, 37–47.

Park, H. G. (2025). Bayesian estimation of covariate assisted principal regression for brain functional connectivity. *Biostatistics*, 26(1), kxae023.

Salvador, R., Suckling, J., Coleman, M. R., Pickard, J. D., Menon, D., & Bullmore, E. (2005). Neurophysiological architecture of functional magnetic resonance images of human brain. *Cerebral Cortex*, 15(9), 1332–1342.

Shen, X., Pan, W., & Zhu, Y. (2012). Likelihood-based selection and sharp parameter estimation. *Journal of the American Statistical Association*, 107(497), 223–232.

Sun, W. W., & Li, L. (2017). STORE: sparse tensor response regression and neuroimaging analysis. *Journal of Machine Learning Research*, 18(135), 1–37.

Van Den Heuvel, M. P., & Pol, H. E. H. (2010). Exploring the brain network: a review on resting-state fMRI functional connectivity. *European Neuropsychopharmacology*, 20(8), 519–534.

Wang, Y., & Guo, Y. (2023). LOCUS: A regularized blind source separation method with low-rank structure for investigating brain connectivity. *The Annals of Applied Statistics*, 17(2), 1307–1332.

Wang, Z., Alahmadi, A., Zhu, D., & Li, T. (2015). Brain functional connectivity analysis using mutual information. In *2015 IEEE global conference on signal and information processing (GlobalSIP)* (pp. 542–546).

Yeo, B. T., Krienen, F. M., Sepulcre, J., Sabuncu, M. R., Lashkari, D., Hollinshead, M., ... others (2011). The organization of the human cerebral cortex estimated by intrinsic functional connectivity. *Journal of Neurophysiology*.

Yu, M., Linn, K. A., Cook, P. A., Phillips, M. L., McInnis, M., Fava, M., ... Sheline, Y. I. (2018). Statistical harmonization corrects site effects in functional connectivity measurements from multi-site fMRI data. *Human Brain Mapping*, 39(11), 4213–4227.

Zhang, R., Chen, L., Oliver, L. D., Voineskos, A. N., & Park, J. Y. (2024). SAN: Mitigating spatial covariance heterogeneity in cortical thickness data collected from multiple scanners or sites. *Human Brain Mapping*, 45(7), e26692.

Zhang, R., Oliver, L. D., Voineskos, A. N., & Park, J. Y. (2023). RELIEF: A structured multivariate approach for removal of latent inter-scanner effects. *Imaging Neuroscience*, 1, 1–16.

Zhao, Y., Wang, B., Mostofsky, S. H., Caffo, B. S., & Luo, X. (2021). Covariate assisted principal regression for covariance matrix outcomes. *Biostatistics*, 22(3), 629–645.

Zhao, Y., & Zhao, Y. (2025). Covariance-on-covariance regression. *Biometrics*, 81(3), ujaf097.

Zonneveld, H. I., Pruim, R. H., Bos, D., Vrooman, H. A., Muetzel, R. L., Hofman, A., ... others (2019). Patterns of functional connectivity in an aging population: The Rotterdam Study. *NeuroImage*, 189, 432–444.

Supplementary materials

A Derivation of Equation (10)

Recall our model is summarized by $\mathbf{Y}_{ij} = \mathbf{U}\boldsymbol{\Pi}_{ij}\mathbf{U}^\top + \mathbf{E}_{ij}$, with $\boldsymbol{\Pi}_{ij} = \text{diag}(a_{ij1}, \dots, a_{ijL})$ and $\mathcal{T}(\mathbf{E}_{ij}) \sim \mathcal{N}(\mathbf{0}, \phi_i^2 \mathbf{I}_p)$. Up to an additive constant, the conditional negative log-likelihood is

$$-\log p(\mathbf{Y}_{ij} | \mathbf{a}_{ij}; \mathbf{U}) \propto \frac{1}{2\phi_i^2} \|\mathcal{T}(\mathbf{Y}_{ij} - \mathbf{U}\boldsymbol{\Pi}_{ij}\mathbf{U}^\top)\|_2^2. \quad (15)$$

Here, we optimize an equivalent form using a Frobenius norm: $\|\mathcal{T}(\mathbf{M})\|_2^2 = \kappa \cdot \|\mathbf{M}\|_F^2$, where κ is a constant that depends only on the choice of $\mathcal{T}(\cdot)$. Since κ does not depend on \mathbf{U} , it does not affect the optimizer. Equation (15) is equivalent (up to constants) to

$$-\log p(\mathbf{Y}_{ij} | \mathbf{a}_{ij}; \mathbf{U}) \propto \frac{1}{4\phi_i^2} \|\mathbf{Y}_{ij} - \mathbf{U}\boldsymbol{\Pi}_{ij}\mathbf{U}^\top\|_F^2. \quad (16)$$

As a preliminary step, let $\hat{\mathbf{a}}_{ij} = \mathbb{E}(\mathbf{a}_{ij} | \mathbf{y}_{ij})$ and $\mathbf{Q}_{ij} = \text{Cov}(\mathbf{a}_{ij} | \mathbf{y}_{ij})$ be the posterior mean and covariance from the E-step. Write

$$\mathbf{a}_{ij} = \hat{\mathbf{a}}_{ij} + \mathbf{d}_{ij}, \quad \mathbb{E}(\mathbf{d}_{ij} | \mathbf{y}_{ij}) = \mathbf{0}, \quad \mathbb{E}(\mathbf{d}_{ij}\mathbf{d}_{ij}^\top | \mathbf{y}_{ij}) = \mathbf{Q}_{ij}.$$

Define $\hat{\boldsymbol{\Pi}}_{ij} = \text{diag}(\hat{a}_{ij1}, \dots, \hat{a}_{ijL})$ so that $\boldsymbol{\Pi}_{ij} = \hat{\boldsymbol{\Pi}}_{ij} + \text{diag}(\mathbf{d}_{ij})$. Then, consider the conditional expectation of the squared Frobenius loss in Equation (16):

$$\begin{aligned} \mathbb{E}[\|\mathbf{Y}_{ij} - \mathbf{U}\boldsymbol{\Pi}_{ij}\mathbf{U}^\top\|_F^2 | \mathbf{y}_{ij}] &= \mathbb{E}[\|\mathbf{Y}_{ij} - \mathbf{U}\hat{\boldsymbol{\Pi}}_{ij}\mathbf{U}^\top - \mathbf{U}\text{diag}(\mathbf{d}_{ij})\mathbf{U}^\top\|_F^2 | \mathbf{y}_{ij}] \\ &= \|\mathbf{Y}_{ij} - \mathbf{U}\hat{\boldsymbol{\Pi}}_{ij}\mathbf{U}^\top\|_F^2 + \mathbb{E}[\|\mathbf{U}\text{diag}(\mathbf{d}_{ij})\mathbf{U}^\top\|_F^2 | \mathbf{y}_{ij}]. \end{aligned} \quad (17)$$

Note that the cross-term vanishes because $\mathbb{E}(\mathbf{d}_{ij} | \mathbf{y}_{ij}) = \mathbf{0}$.

Now, it is sufficient to obtain the second term of Equation (17). Using $\mathbf{U}\text{diag}(\mathbf{d}_{ij})\mathbf{U}^\top = \sum_{l=1}^L d_{ijl} \mathbf{u}_l \mathbf{u}_l^\top$, we obtain

$$\|\mathbf{U}\text{diag}(\mathbf{d}_{ij})\mathbf{U}^\top\|_F^2 = \sum_{l=1}^L \sum_{l'=1}^L d_{ijl} d_{ijl'} (\mathbf{u}_l^\top \mathbf{u}_{l'})^2 = \mathbf{d}_{ij}^\top (\mathbf{U}^\top \mathbf{U} \odot \mathbf{U}^\top \mathbf{U}) \mathbf{d}_{ij}.$$

Taking expectation and using $\mathbb{E}(\mathbf{d}_{ij}\mathbf{d}_{ij}^\top | \mathbf{y}_{ij}) = \mathbf{Q}_{ij}$ yields

$$\mathbb{E}[\|\mathbf{U}\text{diag}(\mathbf{d}_{ij})\mathbf{U}^\top\|_F^2 | \mathbf{y}_{ij}] = \text{tr}((\mathbf{U}^\top \mathbf{U} \odot \mathbf{U}^\top \mathbf{U}) \mathbf{Q}_{ij}). \quad (18)$$

Combining (16), (17), and (18), the M-step objective for updating \mathbf{U} reduces to Equation (10).

B Details of the ADMM algorithm for \mathbf{U} in the penalized M-step

B.1 Penalized M-step objective for updating \mathbf{U} via Equation (12)

Let $\mathbf{Q}_{ij} = \mathbf{Q}_i = \Sigma_{\mathbf{a}_{ij}|\mathbf{y}_{ij}} \in \mathbb{R}^{L \times L}$ denote the conditional covariance of \mathbf{a}_{ij} in the E-step. In our implementation, \mathbf{Q}_i is site-specific and does not depend on j . Define weights $w_{ij} = 1/\phi_i^2$ and $w_{\text{sum}} = \sum_{i=1}^M \sum_{j=1}^{n_i} w_{ij}$. Then the penalized M-step for \mathbf{U} (after one-step linearization of the TLP penalty) can be written as

$$\begin{aligned} \min_{\mathbf{U}, \mathbf{U}^*} \quad & \sum_{i=1}^M \sum_{j=1}^{n_i} \frac{w_{ij}}{2} \{ \|\mathbf{Y}_{ij} - \mathbf{U}^* \mathbf{\Pi}_{ij} \mathbf{U}^{\top}\|_F^2 + \text{tr}((\mathbf{U}^{*\top} \mathbf{U} \odot \mathbf{U}^{*\top} \mathbf{U}) \mathbf{Q}_i) \} \\ & + \lambda \|\mathbf{C}^{(t-1)} \odot \mathbf{U}\|_1 + \lambda \|\mathbf{C}^{*(t-1)} \odot \mathbf{U}^*\|_1 \quad \text{subject to} \quad \mathbf{U} = \mathbf{U}^*, \end{aligned} \quad (19)$$

where $\lambda = \log(n)/2$ in our paper. Following Equation (12), the (v, l) th entry of $\mathbf{C}^{(t-1)}$ are $\frac{1}{\tau} I(|u_{vl}^{(t-1)}| \leq \tau)$, and the entries for $\mathbf{C}^{*(t-1)}$ are defined accordingly.

B.2 ADMM splitting and augmented Lagrangian

To handle the nonsmooth L_1 terms and the symmetry constraint $\mathbf{U} = \mathbf{U}^*$, we introduce auxiliary variables \mathbf{Z} and \mathbf{Z}^* and impose $\mathbf{U} = \mathbf{Z}$, $\mathbf{U}^* = \mathbf{Z}^*$, and $\mathbf{U} = \mathbf{U}^*$. Let $f(\mathbf{U}, \mathbf{U}^*)$ denote the smooth part of (19). We solve

$$\begin{aligned} \min_{\mathbf{U}, \mathbf{U}^*, \mathbf{Z}, \mathbf{Z}^*} \quad & f(\mathbf{U}, \mathbf{U}^*) + \lambda \|\mathbf{C}^{(t-1)} \odot \mathbf{Z}\|_1 + \lambda \|\mathbf{C}^{*(t-1)} \odot \mathbf{Z}^*\|_1 \\ \text{such that} \quad & \mathbf{U} = \mathbf{Z}, \quad \mathbf{U}^* = \mathbf{Z}^*, \quad \mathbf{U} = \mathbf{U}^*. \end{aligned}$$

Using the scaled ADMM form, we introduce dual variables \mathbf{W}, \mathbf{W}^* for $(\mathbf{U} - \mathbf{Z})$ and $(\mathbf{U}^* - \mathbf{Z}^*)$, and $\mathbf{\Lambda}$ for $(\mathbf{U} - \mathbf{U}^*)$. With penalty parameters $\rho > 0$ and $\eta > 0$, the scaled augmented Lagrangian becomes

$$\begin{aligned} \mathcal{L}_{\rho, \eta} = & f(\mathbf{U}, \mathbf{U}^*) + \lambda \|\mathbf{C}^{(t-1)} \odot \mathbf{Z}\|_1 + \lambda \|\mathbf{C}^{*(t-1)} \odot \mathbf{Z}^*\|_1 \\ & + \frac{\rho}{2} \|\mathbf{U} - \mathbf{Z} + \mathbf{W}\|_F^2 + \frac{\rho}{2} \|\mathbf{U}^* - \mathbf{Z}^* + \mathbf{W}^*\|_F^2 + \frac{\eta}{2} \|\mathbf{U} - \mathbf{U}^* + \mathbf{\Lambda}\|_F^2. \end{aligned} \quad (20)$$

B.3 Closed-form updates for \mathbf{U} and \mathbf{U}^*

At iteration k , updating \mathbf{U} reduces to solving

$$\mathbf{U}^{(k+1)} = \underset{\mathbf{U}}{\text{argmin}} f(\mathbf{U}, \mathbf{U}^{*(k)}) + \frac{\rho}{2} \|\mathbf{U} - \mathbf{Z}^{(k)} + \mathbf{W}^{(k)}\|_F^2 + \frac{\eta}{2} \|\mathbf{U} - \mathbf{U}^{*(k)} + \mathbf{\Lambda}^{(k)}\|_F^2. \quad (21)$$

Let \mathbf{G}_{U^*} and \mathbf{H}_{U^*} be defined by

$$\mathbf{G}_{U^*} = \sum_{i=1}^M \sum_{j=1}^{n_i} w_{ij} \mathbf{\Pi}_{ij} (\mathbf{U}^{*\top} \mathbf{U}^*) \mathbf{\Pi}_{ij} \quad \text{and} \quad \mathbf{H}_{U^*} = \sum_{i=1}^M \sum_{j=1}^{n_i} w_{ij} \mathbf{Y}_{ij} \mathbf{U}^* \mathbf{\Pi}_{ij},$$

and define the aggregated conditional second-moment matrix $\bar{\mathbf{Q}} = \frac{1}{w_{\text{sum}}} \sum_{i=1}^M \sum_{j=1}^{n_i} w_{ij} \mathbf{Q}_i$. Then the optimality condition for (21) yields the linear system

$$\mathbf{U}^{(k+1)} \mathbf{K}_{U^*} = \mathbf{H}_{U^*} + \rho(\mathbf{Z}^{(k)} - \mathbf{W}^{(k)}) + \eta(\mathbf{U}^{*(k)} - \mathbf{\Lambda}^{(k)}),$$

where

$$\mathbf{K}_{U^*} = \mathbf{G}_{U^*} + (\rho + \eta) \mathbf{I}_L + w_{\text{sum}} (\mathbf{U}^{*(k)\top} \mathbf{U}^{*(k)} \odot \bar{\mathbf{Q}}).$$

Therefore,

$$\mathbf{U}^{(k+1)} = (\mathbf{H}_{U^*} + \rho(\mathbf{Z}^{(k)} - \mathbf{W}^{(k)}) + \eta(\mathbf{U}^{*(k)} - \mathbf{\Lambda}^{(k)})) \mathbf{K}_{U^*}^{-1}.$$

The \mathbf{U}^* -update is analogous with \mathbf{U} and \mathbf{U}^* swapped.

B.4 Soft-thresholding updates and dual steps

Updating \mathbf{Z} reduces to the following objective:

$$\mathbf{Z}^{(k+1)} = \underset{\mathbf{Z}}{\operatorname{argmin}} \lambda \|\mathbf{C}^{(t-1)} \odot \mathbf{Z}\|_1 + \frac{\rho}{2} \|\mathbf{U}^{(k+1)} - \mathbf{Z} + \mathbf{W}^{(k)}\|_F^2,$$

which has the elementwise soft-thresholding solution

$$Z_{vl}^{(k+1)} = \mathcal{S}_{(\lambda/\rho)C_{vl}^{(t-1)}}(U_{vl}^{(k+1)} + W_{vl}^{(k)}), \quad \mathcal{S}_\kappa(x) = \operatorname{sign}(x) \cdot \max(|x| - \kappa, 0).$$

The update for \mathbf{Z}^* is identical with $(\mathbf{U}^*, \mathbf{W}^*, \mathbf{C}^{*(t-1)})$.

The dual variables are updated by

$$\begin{aligned} \mathbf{W}^{(k+1)} &= \mathbf{W}^{(k)} + \mathbf{U}^{(k+1)} - \mathbf{Z}^{(k+1)}, \\ \mathbf{W}^{*(k+1)} &= \mathbf{W}^{*(k)} + \mathbf{U}^{*(k+1)} - \mathbf{Z}^{*(k+1)}, \\ \mathbf{\Lambda}^{(k+1)} &= \mathbf{\Lambda}^{(k)} + \mathbf{U}^{(k+1)} - \mathbf{U}^{*(k+1)}. \end{aligned}$$

C Supplementary figures for Simulation 2 results

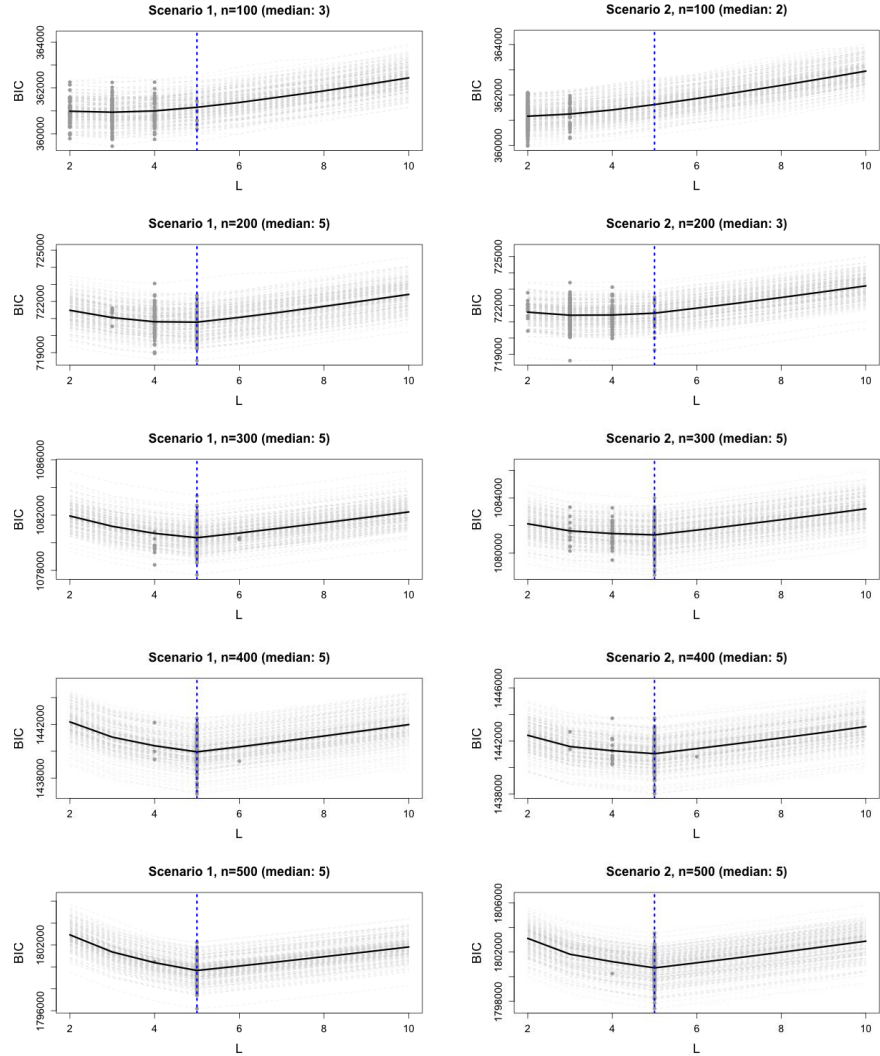


Figure 6: Evaluation of the EBIC criterion in choosing L in simulation studies. Each simulation was repeated 200 times. Each dotted curve and gray dot denote the EBIC curve and its minimum for each simulated data, and the solid curve represents the pointwise average across simulations.